International Journal of Hydrogen Energy 57 (2024) 583–588

Contents lists available at ScienceDirect

International Journal of Hydrogen Energy

journal homepage: www.elsevier.com/locate/he

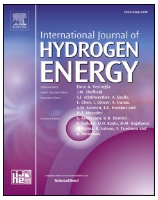

Accurate measurement of hydrogen concentration in transition metal hydrides utilizing electronic excitations by MeV ions

Kristina Komander [*], Paulius Malinovskis, Gunnar K. Pálsson, Max Wolff, Daniel Primetzhofer

Department of Physics and Astronomy, Uppsala University, Box 516, S-751 20, Uppsala, Sweden

ARTICLE INFO

Handling Editor: Umit Demirci

Keywords:
Hydrogen detection
Ion beam analysis
Transition metal hydrides
Hydrogen-rich materials
Electronic excitations
Hydrogen storage

ABSTRACT

This study focuses on enhancing the accuracy of hydrogen content verification in hydrogen-rich ultrathin materials relevant for sustainable energy applications. Ion beams are used for distinctive real-space detection leveraging elastic and inelastic interactions with hydrogen atoms. However, the lack of experimental reference data on electronic interactions poses a challenge to the accuracy of analytical techniques. We investigate the effect of absorbed hydrogen on the electronic energy deposition of ^{15}N-ions in amorphous transition metal compounds, specifically V and Zr, covering concentrations >1H/M. Employing resonant nuclear reactions and Rutherford backscattering, the energy loss is found to increase considerably with hydrogen content, in line with Bragg's additivity. The electronic energy loss cross section for ^{15}N-ions at 6.5 MeV measured (64.55±3.38) eV cm^2/10^{15} atoms. Results are compared to semi-empirical and theoretical models. The findings improve hydrogen profiling accuracy using ^{15}N-nuclear reaction analysis and enable unprecedented methods for hydrogen quantification by other, commonly available ion beams.

1. Introduction

Hydrogen-rich hydrides with transition metals offer reversible hydrogen storage solutions [1–6] and are important for fuel cell applications [7–10], battery electrodes [11,12], and superconductors [13–15]. Their exceptional thermodynamic characteristics support the storage of thermal energy, hydrogen compression, and heating and cooling systems [16–20]. Due to their dynamic optical and electrical properties, they enable sensors, smart mirrors, and windows [21–25].

The interaction of energetic ions with hydrogen in these materials and accurate knowledge of ion energy deposition is critical for various ion beam analysis techniques, including sample depth profiling [26], material modification [27,28], and beam-patterning for nanotechnology [29]. Energetic ^{15}N-ion beams are selectively sensitive to hydrogen with $\sim 10^{18}$ atoms/cm^3 allowing direct concentration measurements via nuclear reaction analysis (NRA) [30] in materials. The concept of depth-resolved NRA is based on the loss of kinetic energy of ^{15}N-ions when traveling through compounds. Hence, understanding and predicting the influence of hydrogen energy loss is essential for hydrogen-containing materials and applications, given ongoing efforts to develop new high-hydrogen-content materials and tailoring properties towards applications. Further, implications extend beyond metal hydrides, encompassing fundamental and diverse aspects of materials science [31–34], including applications in nuclear energy, aerospace, and medical technology. Heavy ion beams like nitrogen are especially effective in cancer therapy [35,36], cosmic ray shielding tests [37], and studies of materials for fusion energy [38].

The continuous loss of kinetic energy in energetic ions passing through matter, known as stopping power $S = \mathrm{d}E/\mathrm{d}x$, primarily arises from interactions with target atom electrons through elastic binary collisions rather than target nuclei. The kinetic energy transfer to the electronic subsystem includes a number of mechanisms that depend in a non-trivial way on the target, the projectile, its velocity, and charge. Target atoms can be excited and ionized by the projectiles, which can in return undergo excitation and change charge states by capture and loss of electrons. Programs like CasP [39] and PASS [40] generate predictions based on theoretical approximations, however, no universal model covers all energies and ion-target combinations. Verification experiments are required and the results are collected in a database by the IAEA [41]. Unfortunately, data is lacking for many ion-target combinations or the available data sets deviate beyond their uncertainties. Semi-empirical tools like SRIM [42] use available datasets to predict energy loss for any ion-target combination and energies. A recent neural network code, ESPNN [43], predicts electronic stopping power using the

---

[*] Corresponding author.
E-mail address: kristina.komander@physics.uu.se (K. Komander).

https://doi.org/10.1016/j.ijhydene.2024.01.032
Received 25 October 2023; Received in revised form 22 December 2023; Accepted 3 January 2024
Available online 12 January 2024
0360-3199/© 2024 The Authors. Published by Elsevier Ltd on behalf of Hydrogen Energy Publications LLC. This is an open access article under the CC BY license (http://creativecommons.org/licenses/by/4.0/).

filtered IAEA database. Still, challenges persist for multi-element targets or changes in aggregation states. Bragg's rule estimates compound stopping powers as weighted mean of elemental standards [44] but in the absence of chemical state effects. All too often deviations from Bragg's additivity occur, particularly in compounds of light elements due to strong hybridization and valence structure changes [45–48]. Furthermore, target aggregation state alterations can induce various simultaneous processes that influence the energy transfer. For example, screening effects by metal conduction electrons on light ion projectiles can decrease the electronic stopping power compared to the gas phase [49,50]. Contrary, for very heavy ions the high density of solid targets influences the charge exchange processes and increases the effective charge state of ions, which correlates to higher stopping relative to the gas phase [51]. Energy loss by hydrogen absorbed in metals might be subject to both chemical and physical state effects. S. Yamaguchi et al. observed that He-ion stopping power was lower for implanted hydrogen in silicon compared to hydrogen in Al-3.5 % Li, where it agglomerates in blisters and is possibly gaseous [52], suggesting a physical state effect. Hydrogen absorbed in transition metals, described as lattice gas [53], induces modifications to their electronic structure, especially in group III metals where metal-insulator transitions may occur [25]. These changes are commonly induced by hybridization between the hydrogen 1s- and metal d-electrons [54]. Therefore, hydrogen's stopping power for heavier ions, i.e., nitrogen, having several charge states at intermediate energies in targets of transition metal compounds, represents a comprehensive precedence, that is studied in this work.

The absence of benchmark data impedes the range and accuracy of analysis methods by means of ion beams and also hampers the advancement of theoretical models and predictive methods. By addressing these gaps in knowledge, our research contributes to paving the way for improved analytical methods and enabling new indirect detection methods accessible at a larger number of laboratories.

2. Experimental methodology

To study hydrogen's impact on ^{15}N-ion energy deposition, the V_xZr_{1-x} metallic glass system was selected as a model system due to its high affinity for hydrogen and good mass contrast. The V_xZr_{1-x} alloys have nominal compositions of $x = 30, 50, 66, 80$ while the variable hydrogen content is not included in the notation throughout this work. Thin films of V_xZr_{1-x} with nominal thicknesses of 400 Å and 500 Å were grown by direct current magnetron sputtering on amorphous SiO_2 substrates and confirmed as amorphous through grazing incidence XRD measurements following the procedure in Ref. [55]. The samples are capped with 6 nm Al_2O_3 to prevent oxidation and hydrogen loss during ion beam analysis [56] and 6 nm Pd to catalyze hydrogen absorption during loading.

Samples are hydrogenated in a temperature-controlled ultra-high vacuum chamber, heated to 150 °C, and exposed to pressures up to 500 Torr of purified hydrogen from a metal hydride. After several hours, the chamber is gradually evacuated and cooled to room temperature. The compounds are expected to remain metallic after hydrogen absorption [55].

Ion beam experiments were done at the 5 MV 15 SDH-2 Tandem accelerator, Uppsala University, Sweden [57]. The composition and areal density of the layers were determined using Rutherford backscattering spectrometry (RBS) with 2 MeV primary ^{4}He-ions. RBS spectra were acquired at incident angles of 5° and 60° to enhance depth resolution. Backscattered ions were detected by a semiconductor detector with a 15 keV FWHM resolution at a 170° scattering angle. Calibration of the energy abscissa was achieved by measuring surface edges on several elemental bulk reference samples. Experimental spectra were analyzed using SIMNRA simulation software [58], utilizing the SRIM-2013 stopping power dataset as preliminary input. Manual iterations were performed to fit spectrum heights and integrals. The accuracy of resulting film areal densities relies on the accuracy of the SiO_2 substrate's stopping power input, as it influences the substrate spectrum's height fitted by the number of impinging particles [26]. Some RBS measurements were charge-normalized by alternating measurements with a thick Cu foil reference of 99.999+% purity over 25 repetitions, hence ensuring equivalent exposure for both samples. The analysis method using Cu as a reference is detailed in Ref. [59]. SRIM-2013's stopping power predictions for ^{4}He-ions on Cu were found to be accurate over a wide energy range. The number of impinging ions on the detector was determined by integrating the backscattering yield near the Cu leading edge, unaffected by surface contaminants, with a relative standard uncertainty below 0.4 %. Subsequently, the RBS spectra of the thin films on SiO_2 were simulated for this number of projectiles. To match the simulation and experiment, stopping powers were manually adjusted through a multiplicative correction factor applied to default predictions, ensuring convergence of the integral count. The universal screening potential was employed for all simulations, with scattering cross-sections based on the Sigma-Calc model.

A measure of the hydrogen density n_H in the films, which is complemented with the hydrogen stopping power in an uncorrelated experiment, is performed by NRA via the $^1H(^{15}N, \alpha\gamma)^{12}C$ nuclear reaction. The ^{15}N-ion beam energy varies between 6.37 and 6.65 MeV, positioning the resonance energy $E_R = 6.385$ MeV at varying depths in the target. Ion fluences were kept below 2 nA. The γ(4.43 MeV) radiation resulting from the nuclear reaction is detected with a Bismuth Germanate scintillation crystal placed outside of the experimental chamber behind the sample [60]. Given the amorphous structure, no channeling effects are considered [61]. The reaction yield vs. incident projectile energy, denoted as $Y(E)$, serves as a relative measure of n_H distribution. $Y(E)$ depends however on the number of impinging ions N, γ-detection efficiency K, and is convoluted with an effective Voigt-shaped instrumental resolution function. This function accounts for broadening effects of the resonant reaction energy range, besides the nuclear resonance width Γ, namely the energy distribution of the incident ion beam, Doppler-effects due to zero-point vibrations, and ion straggling in the target material [20]. Absolute n_H values are determined from $Y(E)$ via numerical deconvolution. The procedure simplifies for a target of homogeneous hydrogen density, where $Y(E)$ remains constant at projectile energies well above E_R and is therefore proportional to n_H [26]:

$$Y(E > E_R) = \frac{\pi}{2} K N \sigma \Gamma \frac{n_H}{S}, \tag{1}$$

where σ is the nuclear resonance cross-section. S depends on the ion energy E. However, the energy loss in surfaces and thin films is relatively small (<0.15 MeV), and therefore, the modification of S is negligible. The experimental setup is calibrated to its characteristic γ-detection sensitivity through a single reference measurement of Y_{ref} and N_{ref} on a sample with known bulk hydrogen density n_{ref} and stopping power S_{ref}. The calibration covers all parameters in eq. (1) other than N, n_H, S_{MH} and is performed on an H-implanted Si-standard of 18.5 % with systematical uncertainty 2–3% which is not included in the analysis procedure. In practice, n_H is obtained by converting $Y(E)$ via:

$$n_H = \frac{Y(E > E_R)}{Y_{ref}} \frac{S_{MH}}{S_{ref}} \frac{N_{ref}}{N} n_{ref} \,. \tag{2}$$

The perceived depth ($d = \Delta E / \Delta S$) and n_H scale with S_{MH}, the stopping power of the investigated material. To a first approximation the stopping cross section of the compound ϵ, the energy loss normalized by the atomic density of the material S/n, can be estimated by the Bragg-rule [44] as a linear combination of its constituent elements' i stopping cross section ϵ_i:

$$\epsilon = \sum_i c_i \epsilon_i = c_V \epsilon_V + c_{Zr} \epsilon_{Zr} + c_H \, \epsilon_H \tag{3}$$

where c_i are the atomic fractions.

A challenge in extracting the stopping cross section of hydrogen ϵ_H in the V/Zr compound is that ϵ, needed to calculate n_H, does itself depend on the hydrogen content c_i. Conventional hydrogen depth profiling is based on solving equations (2) and (3) by an iterative approach, using tabulated values for individual ϵ_i. Several iterations yield consistent values of n_H and S_{MH} [30]. In this study, however, the energy loss in hydrogenated V_xZr_{1-x} films is determined independent of the hydrogen content, by integrating ^{15}N-RBS into the analysis of ^{15}N-NRA yield curves.

Due to its low mass, hydrogen is not directly detectable using ^{15}N-RBS. Instead, we rely on its influence on the stopping power in the V_xZr_{1-x} layer. The hydrogen stopping cross-section is inferred from the backscattering yield of V and Zr atoms, indicated by the height of the backscattering signals and the difference in kinetic energy of ion projectiles backscattered from the top and bottom of a thin film ΔE [16]. Backscattered ^{15}N-ions are detected at a 160° scattering angle using a solid-state detector in the chamber [60]. To extract ϵ_H, SIMNRA simulations [58] are fitted to the recorded spectra incorporating target information from the ^{4}He-RBS analysis. Stopping powers for non-absorbing layers follow the latest SRIM-2013 version, while those in the hydrogenated V_xZr_{1-x} layers remain variable. Manual iterations of the simulation are conducted to achieve agreement of height and width ΔE between experimental and simulated spectra. The detector energy calibration is pre-established through reference measurements, and the projectile number is fitted to the Pd peak. The sole adjustable parameter in the calculations is the multiplicative correction factor for energy loss, which can be determined within an uncertainty of 1.75 % on average. The choice of screening potential models, Anderson or Universal, has a negligible impact on the integral count, so the Universal potential is adopted.

Implementing measured ϵ values, the NRA-yield can be scaled to n_H after converting to S_{MH} with the layer's nominal thickness. Hydrogen-induced lattice expansion is not considered since volume changes cancel out during the analysis, due to normalization by atomic densities, and since the RBS-yield is only sensitive to the layer areal atomic density and not the actual thickness. Finally, equations (2) and (3) are solved to extract ϵ_H in the transition metal compounds:

$$\epsilon_H = \frac{S_{MH} - S_M}{n_H} = \frac{N}{Y_\gamma}\left(\frac{S_{MH} - S_M}{S_{MH}}\right) \bullet K^{'} \tag{4}$$

where calibration parameters for NRA are summarized by $K' = Y_{ref} \cdot S_{ref} / N_{ref} \cdot n_{ref}$ and S_M is the stopping power of the pristine V_xZr_{1-x} layer. The expression depends solely on parameters measured independently in this study. An advantage of this analysis is that uncertainties in nominal thickness or volume changes equally impact both sides of the equation, canceling each other out.

3. Results and discussion

Fig. 1 presents the RBS spectra from V_xZr_{100-x} samples obtained with 2 MeV ^{4}He-ions at 60° incident angle and corresponding simulation by SIMNRA [58]. The analysis of charge normalized spectra reveals an averaged correction factor of 0.965 for the energy loss in SiO_2 relative to the prediction by SRIM-2013, which is consistent with other experiments [62]. This correction is applied to all simulations of ^{4}He-ions in SiO_2 in this work. Additional corrections to the transition metal stopping cross sections are required to accurately reproduce the experimental spectra. For Zr, an average correction factor of 0.841 is needed when using experimental values for V [59]. This correction is reasonable considering experiments on neighboring elements [63]. Hydrogen contaminants in the films, discussed in the following chapter, are estimated to contribute by <1 %. The film composition, denoted as x, remains homogeneous and within 1 at. % of the nominal composition. Target models, containing areal densities and elemental compositions for each layer, were established based on experimental spectra obtained at incident angles of 5° and 60°.

Fig. 2 displays exemplary NRA yield curves for hydrogenated V_xZr_{1-x} samples. The γ-yield is normalized by the relative cumulated ion fluence, without accounting for energy loss or detection efficiency. The flat plateaus within the 6.48–6.55 MeV energy range indicate homogeneous hydrogen distribution in V_xZr_{1-x} layers. Differences in the γ-yield plateau widths are not necessarily due to variations in film thickness but relate to the energy loss since the conversion from ^{15}N-ion energy inversely scales with S_{MH}. While plateau width could serve as a measure of total energy loss in hydrogenated films, it is sensitive to interface effects and becomes challenging for samples with low hydrogen content. The yield curves are averaged over the plateau for n_H analysis.

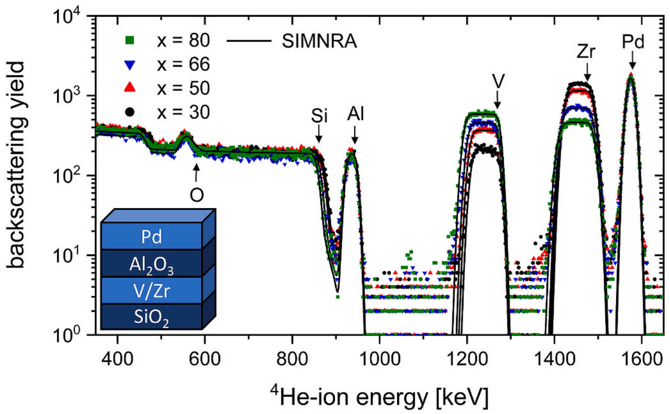

Fig. 1. RBS spectra of 2 MeV primary ^{4}He-ions scattered from 400 Å thick V_xZr_{1-x} thin films with different stoichiometries. The beam incident angle is 60° with respect to the surface normal and the scattering angle is 170°. Solid lines represent fitted simulations using SIMNRA [58]. The inset shows a model of the sample structure.

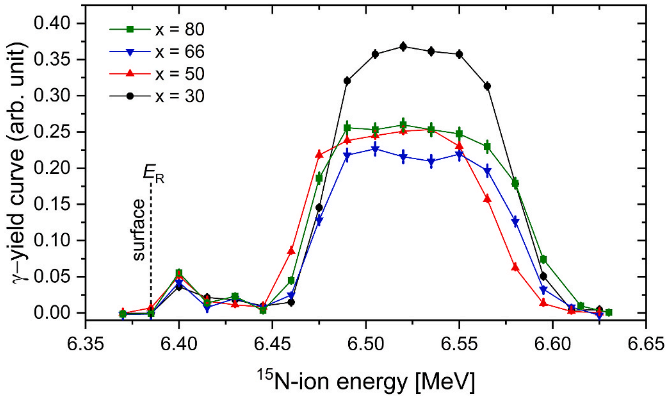

Fig. 2. Excitation curve of the ^{1}H(^{15}N, αγ)^{12}C nuclear reaction resonance from hydrogen-containing V_xZr_{1-x} samples recorded for normal incident angle. The abscissa scales linearly with the stopping power of the individual layers to the probing depth.

Fig. 3 shows subsequently acquired backscattering spectra of 6.6 MeV ^{15}N-ions for a V_xZr_{1-x} layer (x = 66) in its pristine and hydrogen-loaded state. Note that the pristine samples contained trace amounts of hydrogen, as revealed by NRA. SIMNRA simulations are fitted to the experimental spectra, adjusting the multiplicative correction factor for the stopping power of V_xZr_{1-x}. The presence of sharp edges on the lower energy side of the plateaus indicates that plural and multiple scattering events have minor effects, rendering the single scattering approximation in the simulation an accurate representation of the experimental spectra [64]. Differences between the hydrogen-loaded and pristine samples are evident. Hydrogenated V_xZr_{1-x} layers exhibit a wider energy range among backscattered ions, requiring increased energy loss in the simulations corresponding to an increase in total stopping power as absorbed hydrogen atoms contribute their electrons to the compound. Electronic stopping dominates in our case, with the nuclear contribution being less

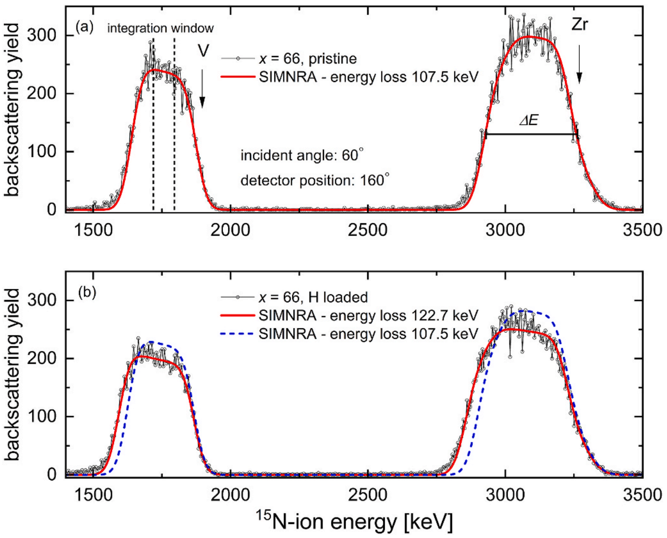

Fig. 3. RBS spectra for 6.6 MeV primary ^{15}N-ions backscattered from (a) pristine and (b) hydrogen-loaded $V_{66}Zr_{33}$ compound for incident angle of 60° and detection angle of 160° (black symbols and line). Simulations using SIMNRA [58] are represented by the thick solid lines. The energy loss in the layer is fitted to the heights, the integral count within the indicated energy range, and the widths *ΔE* of the backscattering plateaus, which corresponds to the difference in kinetic energies of ions scattered from atoms at the top and bottom of the $V_{66}Zr_{33}$ compound.

than 1 % of the electronic stopping cross section for $E/A \gtrsim 100$ keV/u. The distinguishable increase in energy loss with hydrogen concentration in the backscattering spectra suggests the potential for an indirect measurement of hydrogen concentration through the backscattering spectrum, provided accurate energy loss predictions can be achieved.

Fig. 4 summarizes the compound stopping powers S_{MH} determined from simulated total energy loss in V_xZr_{1-x} layers with varying hydrogen content, normalized to film thickness. The values n_H are extracted from NRA yield curves, scaled by individual S_{MH} values. S_{MH} increases linearly with n_H for each material composition x. As the compounds of V and Zr under investigation always contained hydrogen, the electronic stopping cross sections of pure metals ϵ_V and ϵ_{Zr} cannot be directly determined. Hence, extrapolation is applied to datasets spanning a wide n_H range, using linear regression with direct weighting to obtain compound S_M values. Conversion to electronic stopping cross sections [eV cm^2/10^{15} atoms] is accomplished with areal densities and compound composition x. In the inset of Fig. 4, resulting compound electronic stopping cross sections are plotted against x. Following Bragg's additivity rule, a weighted linear regression is performed and extrapolated to x = 0 and x = 1. This yields values of (426.6 ± 12.4) and (521.6 ± 12.74) eV cm^2/10^{15} atoms for pure V and Zr, respectively, deviating by correction factors of 1.018 and 0.854 from SRIM-2013. S_M values are recalculated for each compound x.

Fig. 5 displays the change in stopping power $\Delta S = S_{MH} - S_M$ for the V_xZr_{1-x} compounds as n_H varies. The datasets for different compounds x coincide within their uncertainty, showing a linear increase with n_H. Utilizing eq. (4), the electronic stopping cross section per absorbed hydrogen atom ϵ_H is calculated for each measurement and plotted against n_H in Fig. 5 (bottom). Notably, ϵ_H is itself not dependent on n_H, and a weighted arithmetic mean of values exceeding $4 \bullet 10^{22}$ atoms/cm^3 yields (64.55±3.38) eV cm^2/10^{15} atoms. As the energy loss follows a simple additivity rule for the pure metals and with ϵ_H, the transition metal hydrogen compound is overall perceived as a mixture.

In Fig. 6 the result is compared with literature data and calculated values of ϵ_H over an extended energy range. Literature data from Refs. [65,66], sourced from the IAEA database, pertains to measurements in H_2 gas. Due to significant differences in projectile energy ranges, a direct comparison to evaluate chemical or physical state effects is not feasible. A table in Ref. [26] presents calculated stopping power values for ^{15}N at 6.385 MeV in all elemental targets, suggesting notably smaller stopping power than our experimental findings. Semi-empirical simulations using SRIM-2013 closely approximate our measured value. However, density and gas corrections within SRIM-2013 predict higher losses around and below the Bragg peak, inconsistent with experiments by Ref. [66]. An earlier study involving heavier ions 8<Z<92 in H_2 gas found SRIM considerably underestimating stopping power relative to experimental values [67]. Simulations employing the neural network code ESPNN yield values significantly lower than experimental results. With CasP6.0 [39], ϵ is calculated from the H-1s electrons, scanning over different

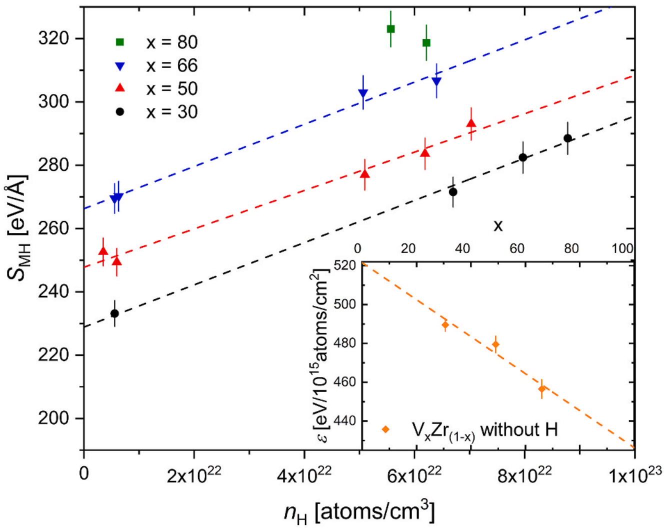

Fig. 4. Experimental stopping power S_{MH} for 6.6 MeV primary ^{15}N-ions in hydrogen-containing V_xZr_{1-x} films versus hydrogen density (filled symbols) and linear regressions (dashed lines). Inset: Stopping cross section ϵ of the hydrogen-free transition metal compounds extracted from extrapolations versus vanadium content *x* (filled symbol) and linear regression (dashed line) to extract ϵ_V and ϵ_{Zr}.

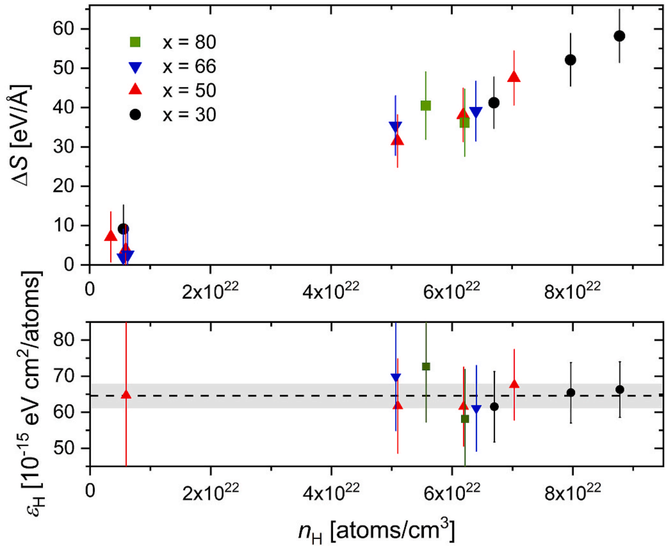

Fig. 5. (top) Experimental stopping power contribution of hydrogen for ^{15}N-ions in different hydrogen-containing V/Zr compounds versus hydrogen densities (filled symbols). Predictions of $\Delta\epsilon$ in hydrogen-containing V/Zr compounds calculated by SRIM-2013 (black dashed line). (bottom) Experimental electronic stopping cross section of hydrogen ϵ_H for ^{15}N-ions versus hydrogen density.

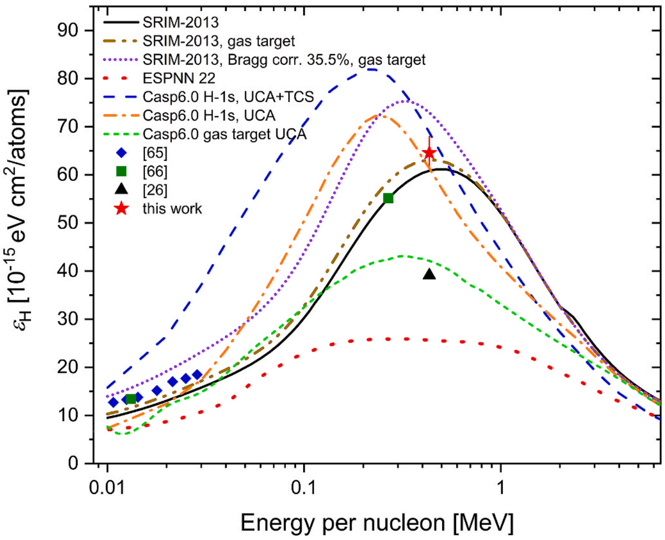

Fig. 6. Experimental electronic stopping cross section of hydrogen with ^{15}N-ions (star symbol) compared to semi-empirical predictions SRIM-2013 [42] and ESPNN [43], theoretical calculations by CasP6.0 [39], and data found in literature.

projectile charge states using the unitary convolution approximation (UCA), both with and without the free-electron-gas approximation model for transport cross section (TCS). Negligible contributions from energy loss due to projectile ionization, excitation, and electron capture are observed in this model. These predictions are reasonably close to the measured value at the investigated projectile energy. CasP6.0's gas target correction predicts much lower energy loss, even below the experimental value [66]. This correction model attributes the lower energy loss to the assumption of a decreased mean projectile charge state in gas targets with lower density, consistent with observations for heavy ions in Ref. [51]. This effect stands in contrast to SRIM and [49], which predict the opposite impact of a change in physical state on energy loss.

It might not be expedient to compare stopping power models that consider 'free' H-1s electrons to the experimentally investigated transition metal hydrogen system. SRIM assumes no changes to electronic structure, while Caps6.0 alters metal core electrons. Neither reflects the hydrogenation process of transition metals [54]. Accordingly, absorbed hydrogen atoms form local bonding states with the transition metals as hybridization between the H-1s electron and valence d-electrons. Bonding states form below the metal d-band, while part of d-electrons lower in energy pushing the Fermi energy upwards [54]. As a rough estimate, the energy loss contributions of individual electron shells of V and Zr using CasP6.0 (UCA+TCS) are considered. This model includes not only approximate changes to the binding energy but also additional screening of ion projectiles and mean charge state changes. The fully occupied V-3p- and Zr-4p-shells show the largest contribution followed by the V-3d, Zr-4d and V-4s, Zr-5s. Single electrons in the V-3d shell contribute with 31.1 eV cm^2/10^{15} atoms and in the Zr-4d shell 41.1 eV cm^2/10^{15} atoms to the energy loss of 6.6 MeV ^{15}N-ions. The total electronic energy loss, including target-induced projectile ionization, excitation, and capture, is 377.9 eV cm^2/10^{15} atoms and 469.31 eV cm^2/10^{15} atoms, respectively, which is 11.4 % and 10.0 % lower than the values determined experimentally in this work. The calculated energy loss contributions by electrons in metal d-shells are lower than by hydrogen s-orbitals, yet smaller than the experimental value. Considering that Casp6.0 produces also smaller total stopping powers of ^{15}N-ions in V and Zr than the experiment, a comparatively smaller size of this rough estimation is not surprising. Nonetheless, out of all the available software, this approximation provides the best description of the H-1s energy loss contribution within the metal system.

4. Concluding remarks

We employed a non-iterative analysis approach using ion backscattering spectra and nuclear reaction yields to reveal the energy transfer between 6.6 MeV ^{15}N-ions and hydrogen atoms in thin film V-Zr alloys. The total electronic energy loss linearly increases with hydrogen content, while nuclear stopping power changes are negligible. After subtracting the energy loss of hydrogen-free samples, datasets for different transition metal compositions align within uncertainties. The energy deposition per absorbed hydrogen atom remains independent of absolute hydrogen content, yielding a weighted arithmetic mean of (64.55 ±3.38) eV cm^2/10^{15} atoms. Including a systematical uncertainty for the detection efficiency calibration of 3 % increases the uncertainty estimation by 1.92 eV cm^2/10^{15} atoms. These results suggest adherence to a simple additivity rule for metals and hydrogen up to H/M∼2. Transition metal hydrides behave as a mixture of V, Zr, and hydrogen. The experimental results show good numerical agreement with calculations by SRIM-2013 or Casp6.0 within the UCA approximation, despite their unsuitable prediction models.

These findings have implications for hydrogen detection by the use of ion beams especially for hydrogen-rich transition metals where hydrogen's energy loss contribution is significant. The compound stopping power, crucial for scaling resonant nuclear reaction yields with ^{15}N-NRA to absolute hydrogen concentration, can be determined accurately on the basis of the results. The study validates the practice of using the simple additivity rule, indicating its applicability to a wide class of materials. Furthermore, they pave the way for novel methods to gauge hydrogen concentration indirectly, such as analyzing Rutherford backscattering spectra employing various ion species without relying on nuclear reactions. This advancement enables quantitative assessment of hydrogen concentrations with an estimated sensitivity to $>10^{22}$ atoms/cm^3 in solids across a wider range of facilities.

Declaration of competing interest

The authors declare that they have no known competing financial interests or personal relationships that could have appeared to influence the work reported in this paper.

Acknowledgments

The authors gratefully acknowledge financial support of the Tandem accelerator infrastructure by VR-RFI (contract #2017-00646_9) as well as the Swedish Foundation for Strategic Research (SSF) under contract RIF14-0053.

References

[1] Schlapbach L, Züttel A. Nature 2001;414:353.
[2] Skintuna B, Lamari-Darkim F, Hirscher M. Int J Hydrogen Energy 2007;32(9):1121–40.
[3] Abe JO, Popoola API, Ajenifuja E, Popoola OM. Int J Hydrogen Energy 2019;44(19):15072–86.
[4] Ma Y, Ma Y, Wan Q, Schweiler S, Botros M, Fu T, Hahn H, Brezesinski T, Breitung B. Energy Environ Sci 2021;14:2883–905.
[5] Marques F, Balcerzak M, Winkelmann F, Zepon G, Felderhoff M. Energy Environ Sci 2021;14:5191–227.
[6] Borgschulte A, Terreni J, Billeter E, Daemen L, Cheng Y, Pandey A, Lodziana Z, Hemley RJ, Ramirz-Cuesta AnJ. Proc Natl Acad Sci USA 2010;117(8):4021–6.
[7] Ma J, Choudhury NA, Sahai Y. Renew. Sust. Energ. 2010;14(1):183–99.
[8] Lototskyy MV, Tolj I, Pickering L, Sita C, Barbir F, Yartys V. Prog Nat Sci 2017;27(1):3–20.
[9] Gkanas EI. Metal hydrides: modeling of metal hydrides to be operated in a fuel cell" in Portable Hydrogen Energy Systems, 67–90. Academic Press; 2018.
[10] Han G, Kwon RK, Kim JB, Lee S, Bae J, Cho E, Lee BJ, Cho S, Park J. Appl Energy 2020;259:113175.
[11] Zhao X, Ma L. Int J Hydrogen Energy 2009;34(11):4788–96.
[12] Wijayanti ID, Denys R, Suwarno, Volodin AA, Lototskyy MV, Guzik MN, Young K, Roven HJ, Yartys V. J Alloys Compd 2020;828:154354.
[13] Ding X, Tam CC, Sui X, Zhao Y, Xu M, Choi J, et al. Nature 2023;615:50–5.

[14] Somayazulu M, Ahart M, Mishra AK, Geballe ZM, Baldini M, Meng Y, Struzhkin VV, Hemley RJ. Phys Rev Lett 2019;122:027001.
[15] Li X, Peng F. Inorg Chem 2017;56(22):13759–65.
[16] Manickam K, Mistry P, Walker G, Grant D, Buckley CE, Humphries TD, et al. Int J Hydrogen Energy 2019;44(15):7738–45.
[17] Sheppard DA, Paskevicius M, Humphries TD, Felderhoff M, Capurso G, Bellosta von Colbe J, et al. Appl Phys 2016;122:395.
[18] Lototskyy MV, Yartys VA, Pollet BG, Bowman Jr RC. Int J Hydrogen Energy 2014;39(11):5818–51.
[19] Sdanghi G, Maranzana G, Celzard A, Fierro V. Renew Sustain Energy Rev 2019;102:150–70.
[20] Muthukumar P, Kumar A, Raju NN, Malleswararao K, Rahman MM. Int J Hydrogen Energy 2018;43(37):17753–79.
[21] Li G, Kobayashi H, Ikeda R, Kubota Y, Kato K, et al. Nat Mater 2014;13:802–6.
[22] Wadell C, Syrenova S, Langhammer C. ACS Nano 2014;8(12):11925–40.
[23] Chen K, Yuan D, Zhao Y. Opt Laser Technol 2021;137:106808.
[24] Palm KJ, Murray JB, Narayan TC, Munday JN. ACS Photonics 2018;5(11):4677–86.
[25] Huiberts JN, Griessen R, Rector JH, Wijngaarden RJ, Dekker JP, de Groot DG, Koeman NJ. Nature 1996;380:231–4.
[26] Lanford WA, Tesmer JR, Nastasi M. Handbook of modern ion beam materials analysis. Mater Res Soc Symp Proc 1995;193.
[27] Talapatra S, Ganesan PG, Kim T, Vajtai R, Huang M, Shima M, Ramanath G, Srivastava D, Deevi SC, Ajayan PM. Phys Rev Lett 2005;95:097201.
[28] Duffy DM, Thomé L, Zhang Y. Curr Opin Solid State Mater Sci 2015;19(1):1–11.
[29] Li J, Stein D, McMullan C, McMullan C, Branton D, Aziz MJ, Golovchenko J. Nature 2001;412:166–9.
[30] Wilde M, Fukutani K. Surf Sci Rep 2014;69:196–295.
[31] Shepard C, Yost DC, Kanai Y. Phys Rev Lett 2023;130:118401.
[32] Jacoby J, Hoffmann DHH, Laux W, Müller RW, Wahl H, Weyrich K, Boggasch E, Heimrich B, Stöckl C, Wetzler H, Miyamoto S. Phys Rev Lett 1995;74:1550. K. Manickam et al., Int. J. Hydrog. Energy 44, 15, 7738-7745, 2019.
[33] Frank A, Ortner A, Bagnoud V, Basko MM, Bedacht S, et al. Nat Commun 2017;8:15693.
[34] Lühr A, Saenz A. Phys Rev 2009;80:022705.
[35] Brown DQ, Seydel HG, Todd P. Cancer 1973;32:541–6.
[36] Durante M, Loeffler J. Nat Rev Clin Oncol 2010;7:37–43.
[37] Guetersloh S, Zeitlin C, Heilbronn L, Miller J, Komiyama T, Fukumura A, Iwata Y, Murakami T, Bhattacharya M. Nucl Instrum Methods B 2006;252(2):319–32.
[38] Renk TJ, Tanaka TJ, Olson CL, Peterson RR, Knowles TR. J Nucl Mater 2004;329–333 A:726–31.
[39] Grande PL, Schiwietz G. Phys Rev 1998;58:3796.
[40] Sigmund P, Schinner A. Nucl Instrum Methods B 2002;195(64).
[41] Stopping power of matter for ions. Computer programs. see, https://www-nds.iaea.org/stopping/stoppingprog.html.
[42] Ziegler JF. SRIM the stopping and range of ions in matter. available at, http://www.srim.org/. accessed 2023.
[43] Haiek FB, Mendez AMP, Monanari CC, Mitnik DM. J Appl Phys 2022;132:245103.
[44] Bragg WH, Kleeman R. Philos Mag 1905;10:318–40.
[45] Ziegler JF, Manoyan JM. Nucl Instrum Methods B 1988;35:215–28.
[46] Thwaites DI. Nucl Instrum Methods B 1992;69(53–63).
[47] Leblanc L, Ross GG, Gollier PA, Bertrand P. Nucl Instrum Methods B 1996;111:17–21.
[48] Roth D, Bruckner B, Undeutsch G, Paneta V, Mardare AI, McGahan CL, et al. Phys Rev Lett 2017;119:163401.
[49] Bergsmann M, Raab W, Schrenk G, Kastner F, Díez Muiño R, Arnau A, Salin A, Bauer P, Echenique PM. Phys Rev B 2000;62:3153.
[50] Bauer P, Semrad D. Adv Quant Chem 2004;46(2):153–63.
[51] Geissel H, Laichter Y, Schneider WFW, Armbruster P. Phys. Lett 99A 1983;(2–3):77–80.
[52] Yamaguchi S, Takahiro K, Nakajima H, Fujino Y, Sagara S, Kamada K, Shiomi-Tsuda N. Nucl Instrum Methods B 1988;33(1–4):163–7.
[53] Lacher JR. Proc R Soc London, A 1937;161:525–45.
[54] Fukai Y. The metal-hydrogen system: basic bulk properties, 21. Springer Science & Business Media; 2006.
[55] Kaplan M, Bylin J, Malinovskis P, Scheicher RH, Pálsson GK. Materialia 2022;24:101496.
[56] Wang Y, Pálsson GK, Raanaei H, Hjörvarsson B. J. All. Com. 2008;464:1–2.
[57] Ström P, Primetzhofer D. J Inst Met 2022;17:P04011.
[58] Mayer M. AIP Conf Proc 1999;475:541–4.
[59] Moro MV, Bruckner B, Grande PL, Tabacniks MH, Bauer P, Primetzhofer D. Nucl Instrum Methods B 2018;424:43–51.
[60] Moro MV, Droulias SA, Müggenburg J, Pálsson GK, Nyberg T, et al. Nucl Instrum Methods B 2019;455:57–60.
[61] Komander K, Tran T, Saha J, Moro MV, Pálsson GK, Wolff M, et al. Phys Rev Lett 2021;127:136102.
[62] Lennard WN, Xia H, Kim JK. Nucl Instrum Methods B 2004;215:297.
[63] Moro MV, Bauer P, Primetzhofer D. Phys Rev 2020;102:022808.
[64] Steinbauer E, Bauer P, Biersack J. Nucl Instrum Methods B 1992;64(1–4):711–5.
[65] Weyl PK. Phys Rev 1953;91:289.
[66] Teplova YA, Nikolaev VS, Dmitriev IS, Fateeva LN. Sov Phys JETP 1962;15:31–41.
[67] Diwan PK, et al. Radiat Meas 2001;33(2):193–202.